NUMERICAL SIMULATION OF GAS-SOLID TWO-PHASE FLOW IN A TOP-FED AIR CLASSIFIER

Xiaochen WU[12], Guangbin DUAN[22], Wenzhen ZHONG[3,*]

This study investigates the gas-solid two-phase flow dynamics and particle classification patterns in a top-fed air classifier through numerical simulations using Fluent software, with a focus on analyzing how rotor cage speed and inlet air velocity collectively influence flow field characteristics and particle separation efficiency. Simulation results revealed that the classification efficiency was significantly improved with the increase of rotor cage speed, but an excessively high rotor cage speed would destroy the stability of flow field. The particle residence time decreased with the increase of inlet air velocity, but the classification efficiency was inferior. An appropriate combination of rotor cage speed and inlet air velocity could effectively guide turbulent airflow of the classifier, further promoting the separation of airflow and particles, and simultaneously improved classification efficiency while boosting the yield of fine powder.

Keywords: Air classifier, CFD, gas-solid two-phase flow, classification efficiency, numerical simulation

1. Introduction

As a fundamental industrial material, when the particle size of powder materials decreases, the surface crystal structure and electronic structure of the particles will undergo changes. Compared with conventional granular materials, fine powders have a large specific surface area, strong magnetism, high activity, strength, reactivity, sensitivity, specificity, stability, thermal conductivity and a series of other unique properties [1]. Their practical applications will become significantly wider. In recent years, the preparation and classification of ultrafine powders with a narrow particle size distribution have garnered more extensive attention [2]. Particle classification is a critical process for obtaining ultrafine powders. Classifiers are widely applied in industries such as mining, construction materials, pharmaceuticals, metallurgy, and chemical engineering due to their stable operation, simple structural design, long service life, and ease of adjustment [3]. Traditional particle classification methods are categorized into dry

[1] School of Materials Science and Engineering, University of Jinan, China, e-mail: 202321201205@stu.ujn.edu.cn
[2] Prof., School of Materials Science and Engineering, University of Jinan, China, e-mail: mse_guangb@ujn.edu.cn
[3]* Prof, School of Mechanical Engineering, University of Jinan , China, (corresponding author) e-mail: me_zhongwz@ujn.edu.cn

classification and wet classification [4]. But the classification of particles is a complex two-phase flow transportation process. Depending on the form of force experienced by the particles in the classification medium (such as gravity, inertia and centrifugal force), the classifier is also mainly divided into gravity classifier, inertia classifier, and centrifugal classifier [5]. According to the direction of the classification airflow field, air classifiers can be categorized into vertical and horizontal types [6]. In addition to the aforementioned classifiers, researchers have also developed novel dynamic classifiers by integrating different types of classification equipment [7]. Currently, researchers mainly focus on two aspects to explore the flow field characteristics and particle distribution of the classifier: (1) experimental analysis (2) numerical simulation.

Experimental analysis can more objectively and truly reflect the classification efficiency of the classifier. Experimental methods such as Laser Doppler Velocimetry (LDV), Particle Image Velocimetry (PIV), Planar Laser-Induced Fluorescence (PLIF), and high-speed photography are generally used to study the internal characteristics of the classifier [8]. Koeninger [9] et al. analyzed the effect of feed concentration and rotor cage speed on fine powder accumulation by combining online detection technology with material testing. Kundu [10] et al. adopted the Central Composite Design (CCD) for experimental design, and utilized the Response Surface Methodology (RSM) to analyze the impact of operating variables on the classification efficiency of the VSK classifier.

Currently, CFD (Computational Fluid Dynamics) has become an alternative method for predicting the internal three-dimensional flow characteristics and turbulent behavior of the classifier [11]. Yang [12] et al. used CFD to simulate the three-dimensional rotating flow field of the classifier and calculated the internal flow field distribution of the classifier under different conditions. Ren [13] et al. added the dispersed phase model (DPM) to the flow field of the classifier to simulate particle trajectories, and verified the impact of the arc-blade rotor cage structure on the improvement of classification efficiency. Yu [14-15] et al. used DPM to further explore the particle distribution patterns in the turbo classifier and later used CFD-DEM (Computational Fluid Dynamics-Discrete Element Method) model to investigate the dispersion effect of the improved guide blade on the fine particle agglomerates in the turbo classifier.

Based on the above two methods, the optimization of classification performance mainly involves two approaches: controlling operating parameters and improving the structure. Huang [16] et al. found that the cut size increased and the distribution of course materials increased as the air velocity increased, the cut size decreased and the distribution of fine materials became denser as the rotational speed increased during the operation of the vertical mill. Esmaeilpour [17] et al. studied the impact of different feed ratios on classification efficiency and energy consumption and found that optimizing feed distribution can

significantly increase the yield of fine powder. Liu [18] et al. designed four types of inclined guide blade models with axial tilt angles of 0°, 2.5°, 5°, and 7.5°, which can effectively reduce the negative impact of upward axial velocity on flow field stability, decrease particle residence time, and improve the dispersion of powder materials. Wang [19] et al. evaluated the classification performance of classifiers with wedge-shaped blades, inverted wedge-shaped blades and main shaft blades based on the entropy generation theory of the second law of thermodynamics and the classifier with wedge-shaped blades has a smaller cut size and higher classification sharpness.

In summary, the entire classification process of the classifier belongs to dilute phase flow, and particle-particle interactions and particle-flow field interactions have a negligible impact on the final results. Implementing the Computational Fluid Dynamics-Discrete Element Method (CFD-DEM) introduces significant computational complexity, resulting in unwarranted resource expenditure. Sun [20] et al. studied the performance evaluation of a horizontal classifier with three rotor cages, and Huang [21] et al. investigated particle motion in vertical roller mills, both employing the Dispersed Phase Model. Based on the research of experts, this study proposes a top-fed air classifier and uses DPM of Fluent software to conduct gas-solid two-phase flow numerical simulation of the flow field and particle field. The classification mechanism of coarse powder and fine powder, fine powder and airflow, as well as the effect of the classifier's operating parameters on the particle classification were revealed by analyzing the effect of the internal velocity and pressure distribution of the classifier on the particle distribution. The results provide novel insights for future structural optimization and design improvements of air classifiers.

The remainder of this paper is organized as follows: Section 2 introduces the theoretical model of the air classifier. Section 3 describes the geometric model of the air classifier. Section 4 presents the preprocessing steps for the numerical simulation. Section 5 discusses the numerical simulation results of the flow field and particle field in the air classifier. Finally, Section 6 summarizes the main conclusions.

2. Theoretical model

2.1 Continuous phase model

According to the fundamental conservation laws of mass and momentum, the governing equations of the flow field can be described as eq. (1) and (2).

$$\frac{\partial \rho}{\partial t} + \nabla \cdot (\rho \vec{u}) = 0 \tag{1}$$

$$\frac{\partial (\rho \vec{u})}{\partial t} + \nabla \cdot (\rho \vec{u} \vec{u}) = -\nabla p - \nabla \cdot \tau_g + \rho g - F \tag{2}$$

In the equations, ρ represents the fluid density, kg/m^3; t represents time, s; $\vec{u}$ represents the average velocity vector of the fluid, p represents the fluid pressure, Pa; τ_g represents the viscous stress tensor of the gas phase; g represents the gravitational acceleration, m/s^2; F represents the external force, N.

The internal flow dynamics within air classifiers during operation exhibit complex flow patterns, including main flow, short-circuit flow, recirculating flow, and eccentric backflow. In engineering, the Standard k-omega turbulence model is often used to simulate the internal flow field of the classifier, and its equations can be described as eq. (3) and (4).

$$\frac{\partial}{\partial t}(\rho k)+\frac{\partial}{\partial x_i}(\rho k u_i)=\frac{\partial}{\partial x_j}\left(\Gamma_k\frac{\partial k}{\partial x_j}\right)+G_k-Y_k+S_k \tag{3}$$

$$\frac{\partial}{\partial t}(\rho\omega)+\frac{\partial}{\partial x_i}(\rho\omega u_i)=\frac{\partial}{\partial x_j}\left(\Gamma_\omega\frac{\partial \omega}{\partial x_j}\right)+G_\omega-Y_\omega+\mathrm{D}_\omega+S_\omega \tag{4}$$

In the equations, k represents the turbulent kinetic energy, j ; x_i , x_j represent the distances in the x and y directions, m; u_i represents the time-averaged velocity in the x direction, m/s; ω represents the turbulent dissipation rate; G_k , G_ω , S_k , S_ω , D_ω represent the production terms of turbulent kinetic energy; Y_k , Y_ω represent the dissipation rate production terms caused by the expansion of compressible turbulent fluctuations.

2.2 Dispersed phase model

The particles are mainly subjected to the joint effects of gravity, drag force, and buoyancy which are followed by Newton's second law, and the differential equation of particle motion can be described as eq. (5), (6), (7) and (8).

$$\frac{du_\mathrm{p}}{dt}=F_\mathrm{D}(u-u_\mathrm{p})+\frac{g(\rho_\mathrm{p}-\rho)}{\rho_\mathrm{p}} \tag{5}$$

$$F_\mathrm{D}=\frac{18\mu}{\rho_\mathrm{p}d_\mathrm{p}^{\,2}}\frac{C_\mathrm{D}Re_\mathrm{p}}{24} \tag{6}$$

$$Re_\mathrm{p}=\frac{\rho d_\mathrm{p}\,|\,u_\mathrm{p}-u\,|}{\mu} \tag{7}$$

$$L=d_\mathrm{p} \tag{8}$$

In the equations, u represents the velocity of the fluid, m/s; u_p represents the velocity of the particle, m/s ; F_D represents the drag force acting on the particle, N; μ represents the dynamic viscosity of the fluid, Pa·s; d_p represents the diameter of the particle, μm; Re_p represents the Reynolds number; C_D represents the drag coefficient; L represents the length scale of the Reynolds number, μm.

3. Geometric model

Fig.1 shows the geometric model of the top-fed classifier. Its primary structure consists of a blower, multi-feed pipe, rotor cage, classification chamber, air distribution chamber, cyclone separator, air collection pipe, and discharge valve. Table 1 presents the main structural sizes of the classifier. The working principle is that the blower provides mixed airflow and spirals downward under the effect of the rotor cage. Powder enters the classifier through the feed pipes and is gradually dispersed by the airflow. The coarse particles collide with the side walls and lose kinetic energy under the effect of a greater centrifugal force from the rotor cage. Then they settle down and are finally discharged from the coarse powder outlet under the influence of gravity and airflow. Fine particles will follow the airflow into the cyclone separator. They will be separated from the airflow at the exhaust pipe and discharged from the bottom of the cyclone separator. A small portion of fine particles will follow the airflow into the exhaust pipe and finally enter the blower to form a closed-loop cycle.

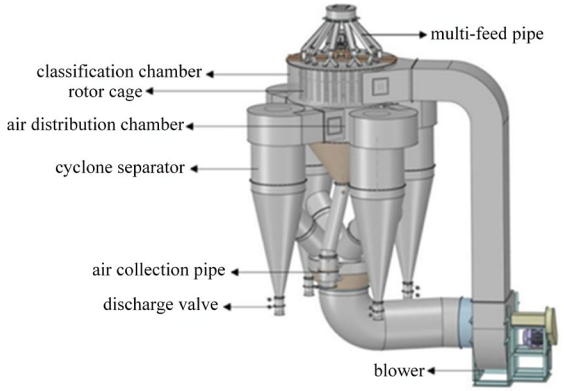

Fig. 1. Geometric model of the classifier

Table 1

Main structural sizes of the classifier

Structural Parameters	Size Values(mm)
Feed inlet diameter	1270
Airflow inlet length	2048
Airflow inlet width	1531
Classifier height	12083
Cage height	1561
Cage diameter	3566
Coarse powder port diameter	750
Fine powder port diameter	342
Exhaust pipe diameter	1160

4. Numerical simulation pre-processing

4.1 Mesh generation

Due to the complex structure of the classifier's geometric model, the classifier was first simplified in SolidWorks. The simplified model is shown in Fig.2. Then the 3D model was imported into SpaceClaim software. The rotor cage was set as the moving area, and other areas as the stationary area. The moving and stationary areas were connected through an interface.

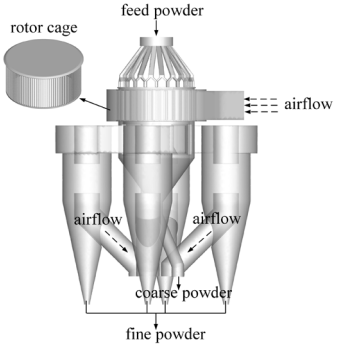

Fig. 2. Simplified model of the classifier

The mesh model of the separator is shown in Fig.3. The mesh near the air inlet and the rotor cage was refined, and the refinement information is shown in Table 2.

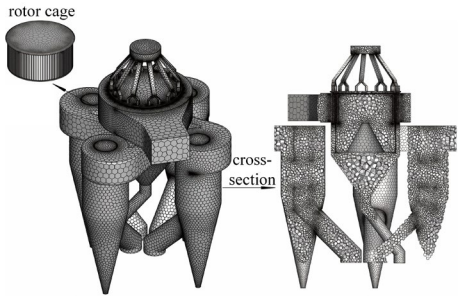

Fig. 3. Mesh model of the classifier

Table 2

Mesh Information

Name	Mesh refinement method	Mesh quantity
Classification chamber	Local refinement	52354
Air distribution chamber		96429
Rotor cage	Local refinement	150163
Air distribution chamber	Local refinement	1783
Air collection pipe		9260

4.2 Boundary conditions and solution methods

The wall boundaries are treated as no-slip boundary. The airflow inlet is defined as velocity inlet, while the airflow outlet is defined as pressure outlet. The particles are randomly generated above the feed pipe. The specific flow field and particle parameter settings for the classifier are detailed in Table 3.

Table 3

Classifier boundary settings

Item	Symbol	Numerical value
Inlet air velocity (m/s)	v_{in}	7-21
Inlet Pressure(Pa)	p_{in}	0
Outlet Pressure(Pa)	p_{out}	0
Rotor cage speed(rpm)	n	150-450
Particle Size (μm)	d_p	5-120
Particle Density (kg/m^3)	ρ_p	2800
Particle Initial Velocity (m/s)	v_p	0

4.3 Model validation

To verify the accuracy and rationality of the numerical simulation results presented in this study, particle size analysis was conducted on graded powder samples using a BT-2001 laser particle size analyzer. As shown in Fig.4, the experimental results showed good agreement with those obtained from the numerical simulations in terms of particle size distribution characteristics. This consistency demonstrates the reliability of the proposed simulation methodology.

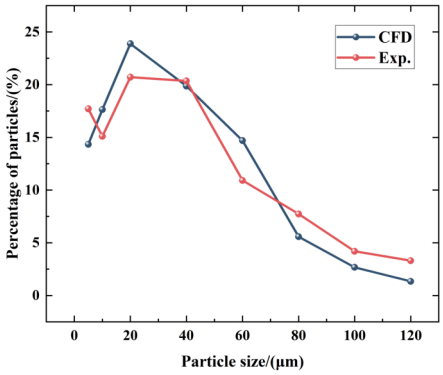

Fig. 4. Comparison between numerical simulations and experimental results

5. Discussions

5.1 Streamline distribution of the classifier

Fig.5 illustrates the airflow distribution characteristics within the classifier under different conditions. Upon entering the classification chamber, the airflow forms an annular flow pattern under the rotor cage's influence, gradually

accelerating toward the central region. After adjustment through the airflow distribution chamber, it spirally enters the cyclone separator. As shown in Fig. 5(b), (d) and (e), increased rotor cage speed enhances the annular airflow effect, causing airflow aggregation near the sidewalls. As shown in Fig.5(a)-(c), excessive inlet airflow velocity induces over-concentrated central airflow with sparse peripheral distribution, compromising flow stability, while insufficient rotation speed fails to effectively guide the airflow, weakening annular circulation. In contrast, the other three conditions demonstrated moderate annular airflow intensity with uniform downward flow distribution, presenting a more rational overall airflow structure conducive to particle classification. Notably, both excessive inlet air velocity and abnormal rotor cage speed may lead to coarse particle entrainment and reduced gas-solid separation efficiency.

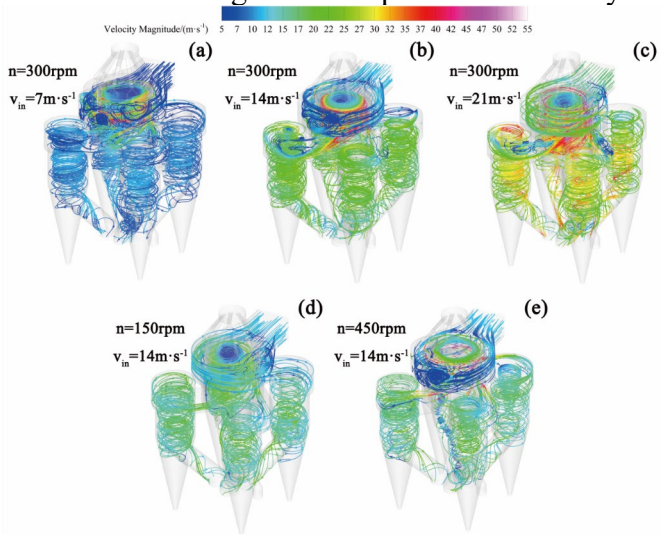

Fig. 5. Velocity streamline distribution under five different operating conditions of (a)n=300 rpm, v_{in}=7 m·s^{-1}; (b)n=300 rpm, v_{in}=14 m·s^{-1}; (c)n=300 rpm, v_{in}=21 m·s^{-1}; (d)n=150 rpm, v_{in}=14 m·s^{-1}; (e)n=450 rpm, v_{in}=14 m·s^{-1}

5.2 Classification area flow field analysis

5.2.1 Velocity and pressure distribution in the classification chamber

Particles undergo dispersion and preliminary classification in the classification chamber. As shown in Fig.6, to investigate the horizontal velocity and pressure distribution characteristics in the chamber, the Z=0.5 m plane of the classifier is selected as the monitoring zone. The airflow external to the guide blades accelerates and enters the rotor cage, forming a dominant clockwise vortex. As shown in Fig.6(a) and (e), compared with the observations in Fig.5, it becomes evident that an increase in rotational speed of the rotor cage may induce adverse effects, such as airflow center deviation. Notably, when the rotational speed

reaches 450 rpm, dual vortex cores emerge, disrupting flow field stability. Additionally, as shown in Fig.6(a)-(c), the increase in inlet air velocity reduces the extent of low-velocity zones and further diminishes the effective operational range at the periphery of the airflow.

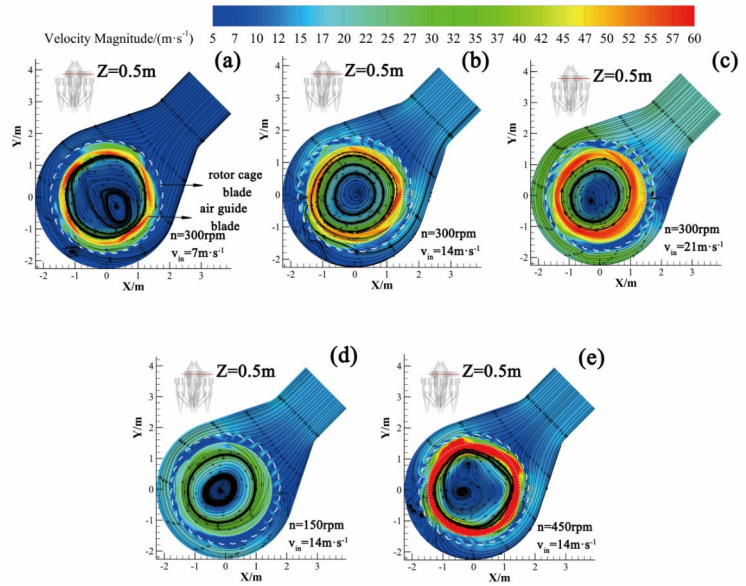

Fig. 6. Velocity contour and streamline distribution at Z=0.5 m under five different operating conditions of (a)n=300 rpm, v_{in}=7 m·s^{-1}; (b)n=300 rpm, v_{in}=14 m·s^{-1}; (c)n=300 rpm, v_{in}=21 m·s^{-1}; (d)n=150 rpm, v_{in}=14 m·s^{-1}; (e)n=450 rpm, v_{in}=14 m·s^{-1}

Fig.7 shows the pressure distribution at Z=0.5 m. The pressure distribution in the classification chamber is significantly influenced by the rotational speed of the rotor cage. Similar to velocity distribution patterns, the synergistic interaction between the rotor cage and guide blades generates high-pressure zones on both sides, while the high-speed rotation of the rotor cage creates a low-pressure region at the chamber center. As the rotor cage speed increases, the central low-pressure zone progressively transitions into a negative-pressure region, accompanied by elevated pressure at the guide blades. This phenomenon amplifies the pressure differential across the rotor cage, thereby enhancing the separation efficiency of coarse and fine particles through intensified aerodynamic drag forces. However, as shown in Fig.7(a)-(c), the rapid airflow simultaneously induces an overall pressure elevation within the chamber. This results in expanded high-pressure regions along the outer periphery of the guide blades and a notable reduction in the spatial extent of the central low-pressure zone.

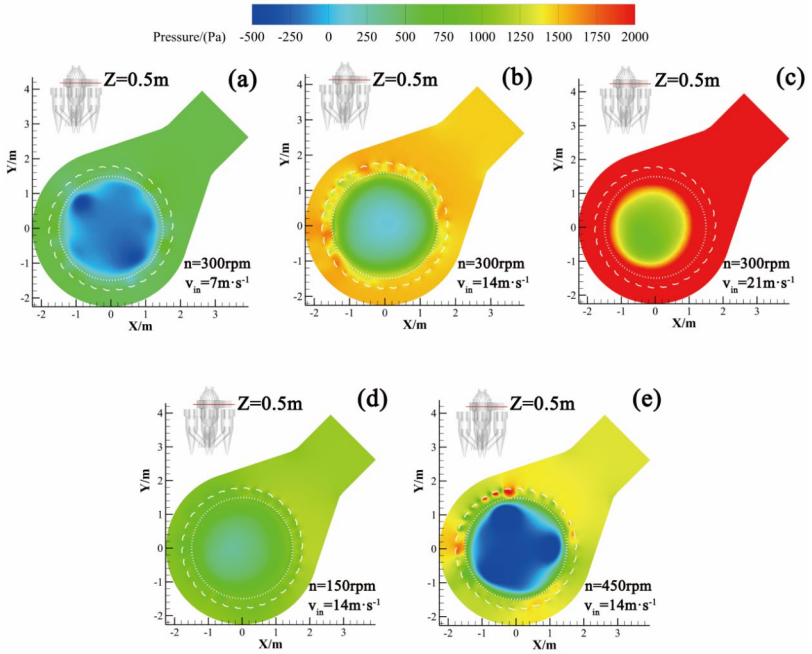

Fig. 7. Pressure distribution at Z=0.5 m under five different operating conditions of (a)n=300 rpm, v_{in}=7 m·s^{-1}; (b)n=300 rpm, v_{in}=14 m·s^{-1}; (c)n=300 rpm, v_{in}=21 m·s^{-1}; (d)n=150 rpm, v_{in}=14 m·s^{-1}; (e)n=450 rpm, v_{in}=14 m·s^{-1}

5.2.2 Radial velocity distribution in the rotor cage

The radial airflow exerts centripetal forces on particles, directing fine particles toward the rotor cage for entry into the cyclone separator, while coarse particles are centrifugally expelled toward the sidewall. Fig.8 demonstrates the role of the rotor cage in the classification of coarse and fine particles. Negative values indicate that the radial velocity direction points towards the center of the rotor cage, while positive values indicate the opposite. Negative radial velocity values dominate at lower rotor cage speeds, whereas increasing rotor speed expands positive values, enhancing particle-wall collisions and suppressing coarse particle entrainment. Concurrently, finer particles exploit dispersed angular pathways to reach the cage center. Inlet air velocity exhibits a non-monotonic influence: moderate velocities amplify inward flow, but excessive velocities disrupt airflow guidance, reducing centripetal dominance and impairing particle separation. Optimal classification occurs when rotor speed and inlet velocity are balanced, which stabilizes aerodynamic classification mechanisms.

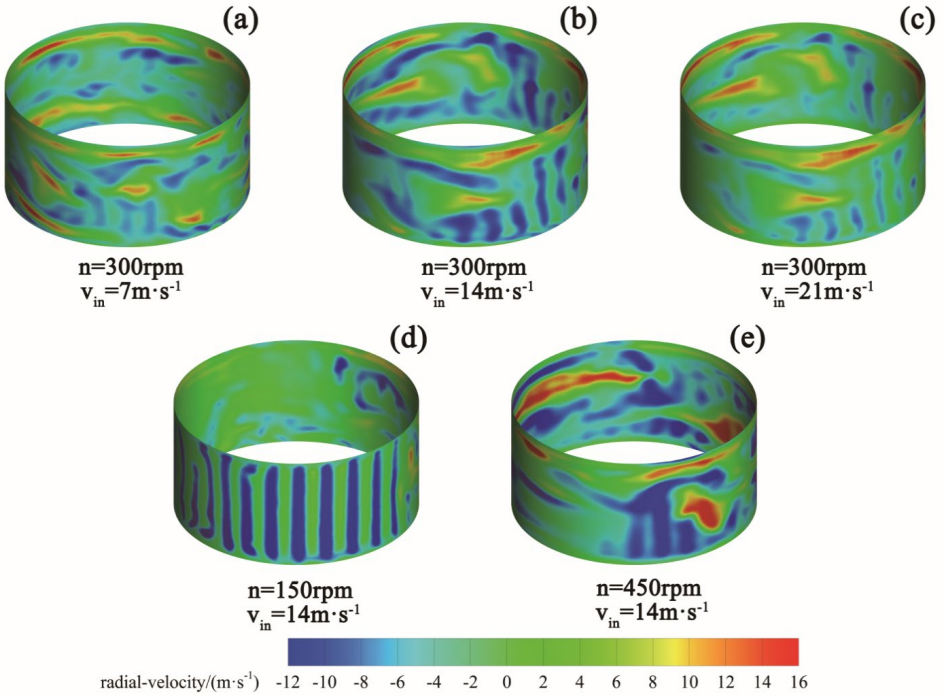

Fig. 8. The radial velocity distribution on outer surface of the rotor cage under five different operating conditions of (a)n=300 rpm, v_{in}=7 m·s^{-1}; (b)n=300 rpm, v_{in}=14 m·s^{-1}; (c)n=300 rpm, v_{in}=21 m·s^{-1}; (d)n=150 rpm, v_{in}=14 m·s^{-1}; (e)n=450 rpm, v_{in}=14 m·s^{-1}

5.2.3 Tangential velocity distribution between blades

As shown in Fig.9, the rotor cage's rotation induces tangential airflow prior to entry, which is critical for uniform particle dispersion. The negative values indicate the same direction of rotation as the cage, while the positive values indicate the opposite. As shown in Fig.9(b), (d) and (e), negative tangential velocities intensify with higher rotor speeds, reaching 60 m/s at 450 rpm versus only 20 m/s at 150 rpm. Table 4 more clearly demonstrates the directly proportional relationship between the blade-edge tangential velocity and the rotor cage speed. As shown in Fig.9(a)-(c), increased inlet air velocity generates counter-rotating tangential flow, while the discrepancy between tangential velocities at the external and internal regions of the blade could induce airflow turbulence, promoting particle back-mixing and non-uniform dispersion.

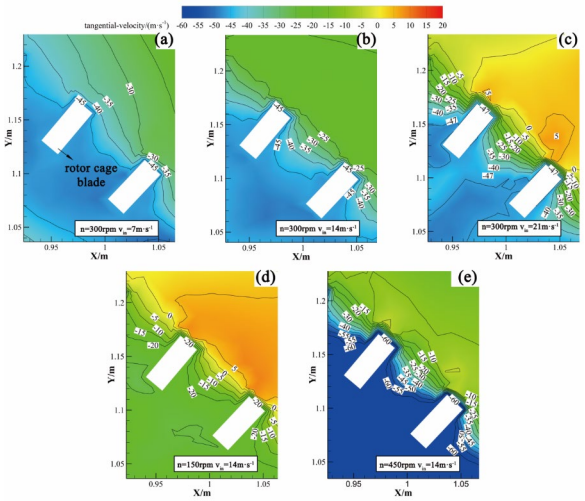

Fig. 9. Tangential velocity distribution between the blades under five different operating conditions of (a)n=300 rpm, v_{in}=7 m·s^{-1}; (b)n=300 rpm, v_{in}=14 m·s^{-1}; (c)n=300 rpm, v_{in}=21 m·s^{-1}; (d)n=150 rpm, v_{in}=14 m·s^{-1}; (e)n=450 rpm, v_{in}=14 m·s^{-1}

Table 4

Blade-edge tangential velocity under different conditions

Operating condition(rpm-m/s)	Blade-edge tangential velocity(m/s)
300-7	45
300-14	45
300-21	47
150-14	20
450-14	60

5.3 Velocity characteristics in air distribution chamber

5.3.1 Horizontal velocity field in air distribution chamber

The air distribution chamber is a critical area for regulating the internal airflow in the air classifier. Deviations in airflow distribution may substantially impact the production yield of fine powder. As shown in Fig.10, to investigate the velocity distribution characteristics of the air distribution chamber, the Z=-0.7 m plane was selected as the monitoring area and the four cyclone separators were labelled clockwise. Under the effect of the air distribution chamber, the airflow is directed into four cyclone separators along a defined trajectory. With the increase of the rotor cage speed, the angle of the airflow entering the cyclone separators will be deflected. When the rotor cage speed increases to 450 rpm, the airflow enters the cyclone separator vertically along the sidewall, forming a high-velocity zone. This configuration leads to increased velocity loss, reduced particle transport capacity, and prolonged particle residence time. Conversely, elevating the inlet air velocity facilitates horizontal airflow entry, resulting in smoother

material transport processes. Simultaneously, the vortex core shifts cyclically from cyclone separators 2 and 3 to separators 1 and 4, with intensified vortex intensity in cyclone separator 2 and diminished strength in separator 4. These dynamic airflow variations may induce non-uniform powder distribution.

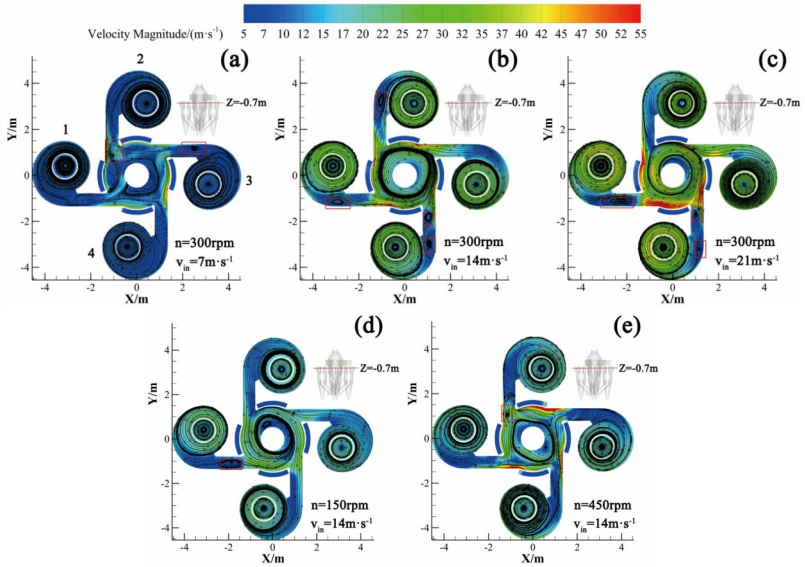

Fig. 10. Velocity distribution in air distribution chamber under five different operating conditions of (a)n=300 rpm, v_{in}=7 m·s^{-1}; (b)n=300 rpm, v_{in}=14 m·s^{-1}; (c)n=300 rpm, v_{in}=21 m·s^{-1}; (d)n=150 rpm, v_{in}=14 m·s^{-1}; (e)n=450 rpm, v_{in}=14 m·s^{-1}

5.3.2 Vertical velocity field in air distribution chamber

The axial airflow velocity reflects the airflow's particle-lifting capacity. Increased upward airflow enhances the drag force exerted on fine particles, reducing their probability of being entrained by coarse particles and consequently improving classification accuracy. Monitoring of axial velocity was conducted for the airflow at the red solid line location at Z=-0.7 m plane in the air distribution chamber. As shown in Fig.11, the axial airflow distribution exhibits significant differences between the left and right zones: In the left zone, airflow turbulence occurs due to the convergence of newly incoming flow with recirculating flow. The upward airflow demonstrates an initial enhancement followed by gradual attenuation as it moves toward the central zone. Under 300-7 and 450-14 conditions, the axial velocity maintains relatively high positive values, whereas other conditions show localized negative values caused by downward airflow interference, resulting in poor particle-lifting effects. In the right zone, axial velocities predominantly transition to negative values as downward airflow accumulates. Under the 300-21 condition, the velocity on the far right reaches approximately -20 m/s. However, the 450-14 condition sustains a positive airflow

of about 10 m/s in the right zone, thus maintaining effective particle-lifting performance.

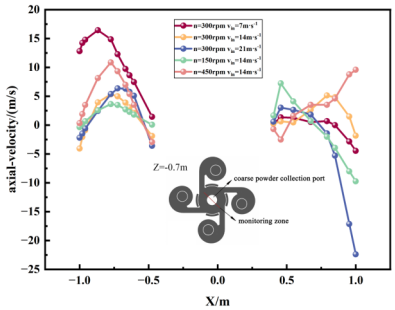

Fig. 11. Axial velocity distribution in air distribution chamber

5.4 Cyclone separator velocity distribution

The velocity distribution of the cyclone separator influences the final fine particle collection efficiency. As shown in Fig.12, the velocity distributions exhibit minor variations across different operating conditions. The airflow tangentially enters and predominantly converges toward the separator center before being discharged through the exhaust pipe. A smaller-diameter recirculation zone with reduced flow velocity forms in the central region, where vortex-induced turbulence facilitates fine particle entrainment into the exhaust pipe. In Fig.12(a), no distinct recirculation zone is observed due to the lower inlet air velocity. When the inlet velocity increases to 21 m/s, localized high-velocity zones emerge near the exhaust pipe due to airflow impingement, accompanied by more concentrated vortices in this region.

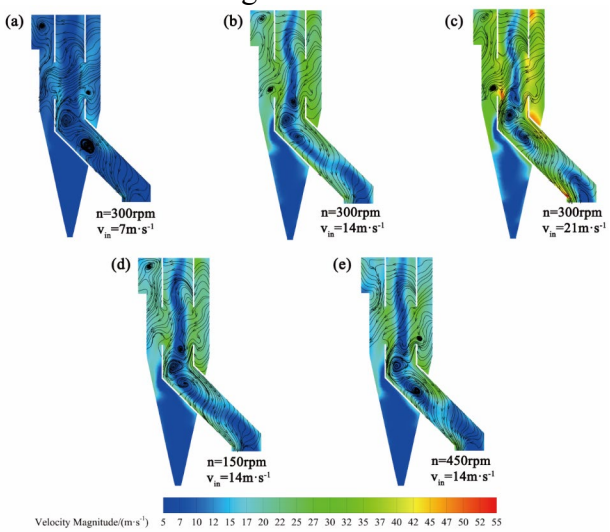

Fig. 12. Velocity distribution in cyclone separator under five different operating conditions of (a)n=300 rpm, v_{in}=7 m·s^{-1}; (b)n=300 rpm, v_{in}=14 m·s^{-1}; (c)n=300 rpm, v_{in}=21 m·s^{-1}; (d)n=150 rpm, v_{in}=14 m·s^{-1}; (e)n=450 rpm, v_{in}=14 m·s^{-1}

5.5 Particle trajectories and characteristics

As shown in Fig.13, the particles enter from the top feed inlet. Under the effect of multiple feed pipes, they fall evenly to the edge of the distributing disc, forming a dispersed state, and finally fall into the classification chamber. Under the effect of internal vortex flows in the classification chamber, specific particles move in a swirling motion. Coarse particles are thrown towards the side walls and lose kinetic energy, finally falling into the coarse powder collection port under the effect of gravity. As shown in Fig.13(c) and (d), within the same time frame, the presence of a relatively fast downward airflow has essentially completed the entire classification process. However, there is a significant amount of coarse particles entering the cyclone separator. As shown in Fig.13(a), (b) and (e), due to the better lifting effect of the airflow on the particles, the entire classification process proceeds more slowly. There are still particles remaining in the feed hopper. However, fewer coarse particles are drawn into the cyclone separator, resulting in a relatively high overall classification accuracy. In summary, while ensuring high classification accuracy, the completion time of the entire classification process may increase.

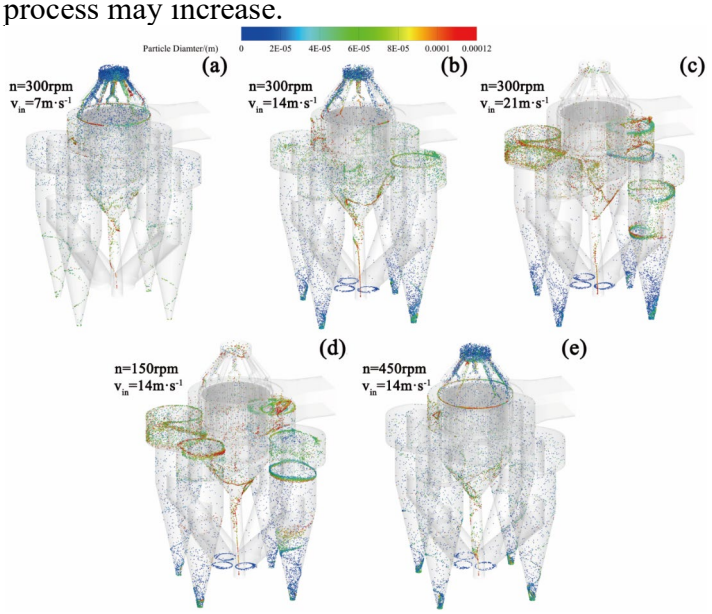

Fig. 13. Particle trajectories under five different operating conditions of (a)n=300 rpm, v_{in}=7 m·s^{-1}; (b)n=300 rpm, v_{in}=14 m·s^{-1}; (c)n=300 rpm, v_{in}=21 m·s^{-1}; (d)n=150 rpm, v_{in}=14 m·s^{-1}; (e)n=450 rpm, v_{in}=14 m·s^{-1}

As shown in Fig.14 (a), due to uneven airflow entering the four cyclone separators, there are also significant differences in the fine powder yield of the cyclone separators. Under the 300-14, 300-21, and 150-14 conditions, the powder feeding process is relatively smooth, but the powder yield is more affected by vortex. The vortex at the inlet of cyclone separator 3 is relatively small, and the

powder yield is much higher than that of the other three cyclone separators. The difference in powder yield among the other three cyclone separators is not significant. In the conditions of 300-7 and 450-14, the velocity loss of the airflow at the side wall is relatively large, and the overall powder yield is less affected by vortices. The particle number distribution is relatively uniform. Fig.14 (b) shows the classification efficiency curve of the classifier. Under the 300-7 condition, the entire curve is at the top, and the classification efficiency for 120 μm particles can reach about 80%, indicating the best classification effect. The classification effect is also good under the 300-14 and 450-14 conditions, which can reach about 70%. However, the classification effect under the 450-14 condition is suboptimal, likely due to the excessively high rotational speed of the rotor cage, which destabilizes the flow field and prolongs particle residence time in the classifier. This increases the probability of coarse particles being entrained into the cyclone separator. In contrast, under the 150-14 and 300-21 conditions, insufficient rotor cage rotational speed or excessive downward airflow velocity hinders effective dispersion of coarse and fine particles. Consequently, substantial coarse particles are carried into the cyclone separator, significantly compromising classification efficiency. Notably, the partial classification efficiency for 120 μm particles drops to approximately 25% in these conditions. As clearly demonstrated in Table 5, the percentage distribution of particle sizes in collected fines varies significantly under different operating conditions. Particles measuring 10-60 μm constitute the dominant fraction across all conditions, consistently accounting for approximately 15% of the total. Notably, the ultra-fine particle fractions show significantly higher proportions under the 300-7, 300-14, and 450-14 conditions. In contrast, the 300-21 and 150-14 conditions exhibit a noticeable increase in coarse particle percentages accompanied by a corresponding reduction in fine particle fractions.

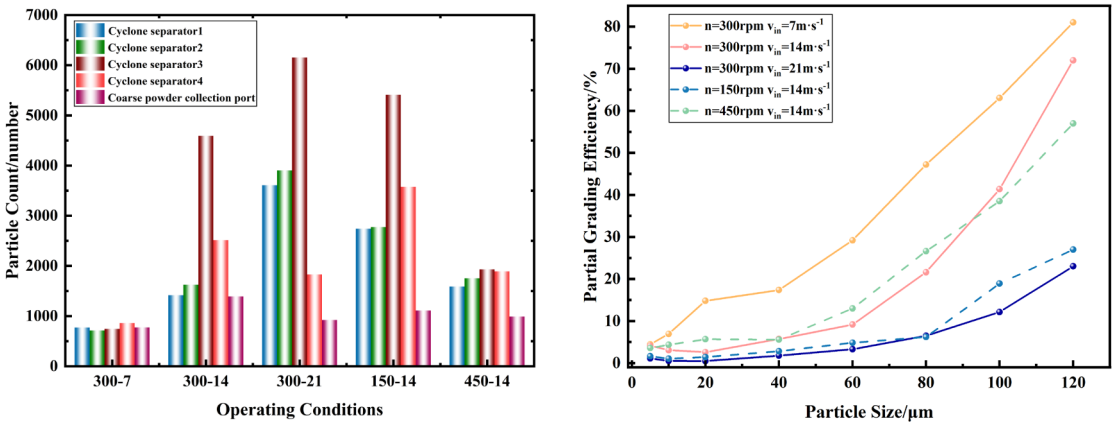

(a) Particle distribution (b) Particle classification efficiency

Fig. 14. Particle classification effect

Table 5

Percentage distribution of particle sizes in the fine powder collection port

Operating condition(rpm-m/s)	Particle size(μm)							
	5	10	20	40	60	80	100	120
300-7	18.13	21.30	24.99	18.16	10.13	4.89	1.65	0.74
300-14	9.18	14.96	23.40	20.50	15.83	10.09	4.81	1.23
300-21	6.54	13.08	17.53	14.53	14.85	13.86	11.50	8.11
150-14	7.98	11.79	18.42	15.92	14.98	13.61	10.44	6.85
450-14	14.33	17.64	23.88	19.87	14.69	5.57	2.67	1.34

6. Conclusions

This study utilized Fluent software to simulate the flow field and particle field of a classifier under five conditions. The investigation focused on the effects of rotor cage speed and inlet air velocity on the flow field characteristics and classification performance of the classifier. The main findings are summarized as follows:

(1) The toroidal airflow within the rotor cage became intensified with the increase of rotor cage speed. Correspondingly, the spiraling downward airflow in the cyclone separator becomes increasingly vigorous and dense with an increase of inlet air velocity.

(2) Increasing the rotor cage speed will increase the velocity difference and pressure difference of the classification chamber. An appropriate pressure difference and velocity difference will enhance the separation of air and particles, further improving the classification efficiency.

(3) The vortices in the air distribution chamber can lead to differences in the air volume entering different cyclone separators, which in turn can cause differences in particle yields. As the rotor cage speed increases, a strong upward airflow is generated in the air distribution chamber, enhancing the lifting effect on the particles.

(4) The vortices in the cyclone separator increase the residence time of the finished particles within the separator. Some of the finished particles may also escape through the exhaust pipe with the vortices, reducing the classification accuracy.

(5) The classification efficiency is best under the 300-7 condition, and the yield of fine powder is relatively low. Considering the comprehensive analysis of classification efficiency and particle yield, 300-14 is the optimal parameter selection.

REFERENCES

[1] *Sadhasivam S, Shanmugam M, Umamaheswaran P D, et al.* Zinc oxide nanoparticles: green synthesis and biomedical applications. Journal of cluster Science, 2021, 32(6): 1441-1455.

[2] *Gu Yinan, et al.* Air supply structure design and flow field simulation of turbo air classifier. China Powder Science and Technology, 30.05 (2024): 158-170.

[3] *Zhang Yu, Liu Jiaxiang, Yang Ru*. Review and Prospects of Turbo Air Classifiers. China Powder Science and Technology, 05(2003): 37-42.

[4] *Pukkella, Arjun Kumar, Jan J. Cilliers, and Kathryn Hadler*. A comprehensive review and recent advances in dry mineral classification. Minerals Engineering 201 (2023): 108208.

[5] *Shapiro, M., and V. Galperin*. Air classification of solid particles: a review. Chemical Engineering and Processing: Process Intensification 44.2 (2005): 279-285.

[6] *Sun Zhanpeng, et al.* Status and advance in centrifugal airclassifiers. China Powder Science and Technology 23. 02 (2017): 39-43.

[7] *Lu Daoming, FAN Yiping, LU Chunxi*. Advances in research on granular air classification. China Powder Science and Technology, 2020, 26(6): 11-24.

[8] *Fu Min, et al.* Research progress of air classification technology and equipment. Chemical Industry and Engineering, 41.04(2024): 117-130.

[9] *Koeninger, Benedikt, et al.* Classifier performance during dynamic fine grinding in fluidized bed opposed jet mills. Advanced Powder Technology 30.8 (2019): 1678-1686.

[10] *Kundu, Tonmoy, et al.* Performance evaluation of the VSK separator for treating mineral fines. Minerals Engineering 167.11(2021):106883.

[11] *Guo, Ming, et al.* An overview of novel geometrical modifications and optimizations of gas-particle cyclone separators. Separation and Purification Technology329(2024):125136.

[12] *Yang Qingliang and Liu Jiaxiang*. Numerical simulation and measurement of three-dimensional flow field in turbo air classifier. Chemical Engineering, 37.01(2009): 24-27.

[13] *Ren Wenjing, Liu Jiaxiang, Yu Yuan*. Design of Rotor Cage with Arc-blade for the Turbo Air Classifier. Journal of Mechanical Engineering, 52.02(2016): 195-201.

[14] *Yu Yuan, et al*. Study of particle motion and distribution laws in the turbo air classification flow field. CIESC Journal, 74.10(2023): 4074-4086.

[15] *Yu, Yuan, et al.* Influence of guide blade on dispersion of aggregates near the guide blade in a turbo air classifier. Powder Technology 434 (2024): 119344.

[16] *Huang, Rongjie, et al.* Operation parameters multi-objective optimization method of large vertical mill based on CFD-DPM. Advanced Powder Technology 34.6 (2023): 104014.

[17] *Esmaeilpour, Mohamadreza, Ali Mohebbi, and Vahab Ghalandari*. CFD simulation and optimization of an industrial cement gas–solid air classifier. Particuology 89 (2024): 172-184.

[18] *Liu, Rongrong, Jiaxiang Liu, and Yuan Yu.* Effects of axial inclined guide blades on a turbo air classifier. Powder Technology 280 (2015): 1-9.

[19] *Wang, Zhiyuan,et al.* Structure optimization of rotor cage blades for turbo air classifier based on entropy production analysis. Advanced Powder Technology 34.8 (2023): 104103.

[20] *Sun, Zhanpeng, et al.* Orthogonal vortices characteristic, performance evaluation and classification mechanism of a horizontal classifier with three rotor cages. Powder Technology 404 (2022): 117438.

[21] *Huang, Rongjie, et al*. Operation parameters multi-objective optimization method of large vertical mill based on CFD-DPM. Advanced Powder Technology 34.6 (2023): 104014.